Lithos 324–325 (2019) 626–639

Contents lists available at ScienceDirect

Lithos

journal homepage: www.elsevier.com/locate/lithos

The effect of P–T on the reaction between tonalitic melt and mantle lherzolite at 2–4 GPa and implications for evolution of North China Cratonic Lithosphere and generation of High Mg# andesite

Mingliang Wang [a,b,c], Chunjuan Zang [a,b,c], Hongfeng Tang [a,*]

[a] Key Laboratory for High Temperature and High Pressure Study of the Earth's Interior, Institute of Geochemistry, Chinese Academy of Sciences, Guiyang, 550081, PR China
[b] Suzhou University, Suzhou, Anhui 234000, PR China
[c] Anhui Engineering and Technological Research Center for Coal Exploration-China, Suzhou 234000, PR China

ARTICLE INFO

Article history:
Received 16 July 2018
Accepted 27 November 2018
Available online 4 December 2018

Keywords:
Melt–peridotite reaction
High-Mg# andesite
North China Craton
Mantle xenolith

ABSTRACT

To assess the effects of reaction factors (mainly P and T) on the mineral assemblage and chemical composition of residual minerals and reacted melt in the reaction between andesitic melt and mantle peridotite, we conducted experimental reactions between tonalitic melt and mantle lherzolite using a DS-3600 six-anvil apparatus at 2–4 GPa and 1250 °C–1400 °C. The reaction products contain two types of reaction vein: orthopyroxene (r) [r means this mineral generated in melt-peridotite reaction and located at reaction rim] + garnet(r) and orthopyroxene(r). The mineral assemblages of the reaction veins are controlled by the reaction P and T, which can be determined via the empirical discriminant function: $Y = 3.33 \times 10^{-6} T^2 - 2.17 \times 10^{-3} T - 0.5 - P$ (T in °C, P in GPa; $Y \geq 0$: Opx veins form; $Y < 0$: Opx + Grt veins form). These two types of reaction vein match those found in mantle xenoliths in Mesozoic and Cenozoic magmas from the North China Craton (NCC), indicating that they were formed by similar processes. The melt–peridotite reaction (including P and T) also influences the chemical composition of the residual minerals in the experimental products, with the major element variations being similar to those of NCC lithospheric mantle evolution from Palaeozoic to Cenozoic. Based on the experimental results, olivine in xenoliths from depths of ~100 km (~3 GPa) has higher SiO_2 and lower NiO and MnO contents than olivine in xenoliths from depths of ~130 km (~4 GPa), and orthopyroxene in xenoliths from depths of ~100 km has higher Mg#, higher CaO content, and lower NiO content than orthopyroxene in xenoliths from depths of ~130 km. The reacted-mantle xenoliths contain clinopyroxene that originated from cold (<1300 °C) and deep (~135 km) lithospheric mantle. The P–T conditions also control the chemical composition of the reacted melt. An increasing reaction pressure increases the SiO_2 content, whereas an increasing reaction temperature reduces the SiO_2 content. In combination with the varying Na_2O and K_2O contents of the parental magma, the reacted melt can yield almost all types of intermediate magma with high Mg# (Mg# = mol[Mg/(Mg + $\sum$Fe)], Mg# > 0.45) character. This variation in major element of the reacted melt agrees with field observations of Mesozoic high-Mg# andesitic rocks from the NCC, indicating similar causes of the variation in the major element contents. With respect to the trace element content of the reacted melt, a garnet content of 15%–20% produces a right deviation of the heavy rare earth element partition curve (chondrite-normalized) and substantially elevates the Sr/Y and La_N/Yb_N ratios, indicating an adakite-like reacted melt.

1. Introduction

The generation of high-Mg# (Mg# = mol[Mg/(Mg + $\sum$Fe)], Mg# > 0.45) andesites (HMAs) is associated mainly with the reaction between silicic melt and mantle peridotite (Kelemen, 1995), which is affected by the reaction pressure (P) and temperature (T). These melt–peridotite reactions under the different P–T conditions found in dissimilar geotectonic settings might be key influences on the evolution of the lithospheric mantle, including on the evolution of Mesozoic HMAs from the North China Craton (NCC, Fig. 1). These HMAs have the following typical features: (1) their SiO_2 content varies from 53 to 68 wt% and their $K_2O + Na_2O$ content varies from 4 to 10 wt%, covering almost all types of intermediate rock; (2) they are enriched in Sr and Pb, depleted in Y and high field strength elements (HFSEs), and contain inherited Archaean zircons (Gao et al., 2004; Huang et al., 2007a; Wu et al., 2003; Xu et al., 2006b; Yuan et al., 2006); and (3) they contain abundant xenoliths and xenocrysts, which originate from the mantle, as inferred from their textures (e.g., protogranular texture and porphyroclastic texture) and chemical compositions (e.g., enriched in Mg, Cr, Ni, Co;

* Corresponding author.
E-mail address: tanghongfeng@vip.gyig.ac.cn (H. Tang).

https://doi.org/10.1016/j.lithos.2018.11.035
0024-4937/

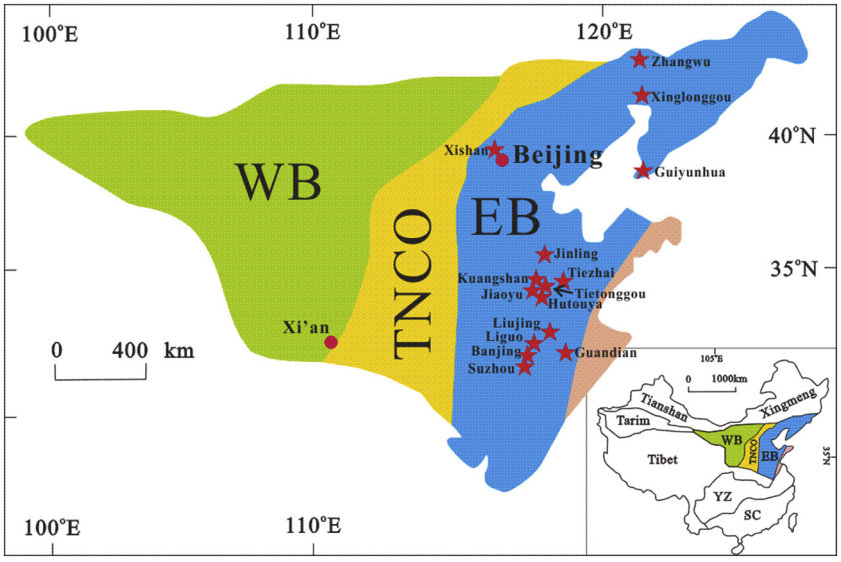

Fig. 1. Mesozoic high Mg# andesitic magmatic rocks in North China Craton. Schematic geologic map of the North China Craton is after Wu et al. (2008) and Wang et al. (2013). WB (Western Block), TNCO (Trans-North China Orogen), and EB (Eastern Block), these tectonic divisions are after Zhao et al. (2001). The location of reported HMAs (Chen et al., 2013; Gao et al., 2004; Huang et al., 2007a; Ma et al., 2016; Wu et al., 2003; Xu et al., 2006b; Xu et al., 2008; Xu et al., 2009; Yang, 2007; Yuan et al., 2006; Zi et al., 2007) are shown as red stars.

depleted in Sr, Ba) (Chen and Zhou, 2004; Chen and Zhou, 2005; Wang et al., 2012; Xu et al., 2008; Xu et al., 2010a).

The NCC HMAs were produced during the period when the NCC lost its cratonic lithospheric keel (Gao et al., 2008; Menzies et al., 1993; Xu, 2001), suggesting a genetic relationship between HMA generation and lithospheric keel loss (Zhang, 2005; Zhang et al., 2007). There are three main hypotheses regarding the generation of Mesozoic HMAs in the NCC: HMAs were produced by (1) intermediate magma that was derived from the partial melting of delaminated continental crust and contaminated by mantle rocks (Gao et al., 2004; Xu et al., 2008), (2) magma that was derived from strongly hydrated lithospheric mantle contaminated by silicic melt derived from continental crust (Ma et al., 2016; Wu et al., 2003), or (3) magma that was derived from the mixing of mantle-derived basic magma and silicic melt derived from the partial melting of continental crust (Chen et al., 2013). Each of these hypotheses needs to be able to explain the above-mentioned geological characteristics of HMAs, which we summarize as follows. With respect to hypothesis (1), the melt from delaminated Archaean continental crust should be enriched in Sr and Pb, depleted in Y and HFSEs (the attribution of continental crust), and contain abundant inherited zircons. Based on the melt–peridotite reaction, the MgO and mantle xenolith/xenocryst contents of the melt should increase during magma ascent, that is, the major element contents should change during such ascent (Gao et al., 2009). With respect to hypothesis (2), the melt from hydrated lithospheric mantle should have a variable major element content (including high MgO content) and a continental crust signature as a result of the contaminated magmatic source. In addition, Archean zircons would be destroyed in hot lithospheric mantle. Although some Archaean zircons could be inherited from a shallow crust during magma ascent, it is difficult to explain the reasonably uniform Archaean zircon contents found in most of the Mesozoic HMAs from the inner NCC; With respect to hypothesis (3), more than two endmembers are needed to produce the various different types of intermediate rock. However, the temperatures and viscosities of mafic and silicic melts differ, and considering more than two endmembers would make a mixing process unlikely. Given the above, hypothesis (1) appears to be best able to explain the generation of HMAs. That is, HMAs might be generated during the reaction between intermediate magma [perhaps similar to tonalite–trondhjemite–granodiorite (TTG), generated from the partial melting of delaminated eclogite] and mantle peridotite.

However, some key aspects of this important reaction remain unexplored, including the following with regard to HMAs of the NCC: (1) the relationship between the melt–peridotite reaction P–T and the mineral assemblage of the reaction veins of mantle xenoliths, (2) the relationship between the melt–peridotite reaction P–T and the chemical composition variation of lithospheric mantle from Palaeozoic to Cenozoic, and (3) the relationship between the melt–peridotite reaction P–T and the chemical composition variation of Mesozoic HMAs from the inner NCC. These relationships should be established to better understand the cause of the heterogeneity of the mineral assemblage and chemical composition of Mesozoic and Cenozoic mantle xenoliths from the inner NCC, the reason for the variation in the chemical composition of the HMAs, and the spatiotemporal variations in the properties of the NCC Mesozoic lithospheric mantle. Such knowledge would help to understand the cause of the loss of cratonic lithospheric mantle of the NCC during the Mesozoic.

To investigate the relationship between the reaction P–T and magma/xenolith composition, many studies have focused on field observations (Sun et al., 2012; Zheng et al., 2016). However, it is difficult to reliably determine this relationship via field observations alone because field samples might be affected by late geological processes. And these relationships can be investigated through experimental studies and then comparing the reaction products with field observations. Many experimental studies have been performed to investigate the reaction between intermediate magma and mantle peridotite (Gao et al., 2017; Johnston and Wyllie, 1989; Lambart et al., 2012; Rapp et al., 1999; Rapp et al., 2010; Sekine and Wyllie, 1982; Wang et al., 2010; Wang et al., 2013; Wang and Tang, 2013; Yaxley and Green, 1998). Several of these studies investigated melt–peridotite reaction in the NCC. For example, Wang et al. (2010) studied the reaction between andesitic melt and peridotite at 1250 °C–1400 °C and 2 GPa and obtained high-Mg# magma and lherzolite [residual mineral phase composition: orthopyroxene (Opx) + olivine (Ol) + clinopyroxene (Cpx) + Opx(r) + Cpx(r), where r represents the reaction rim, that is, the mineral phase formed during the reaction]. Wang et al. (2013) performed a dissolution experiment with basaltic andesite and spinel lherzolite at

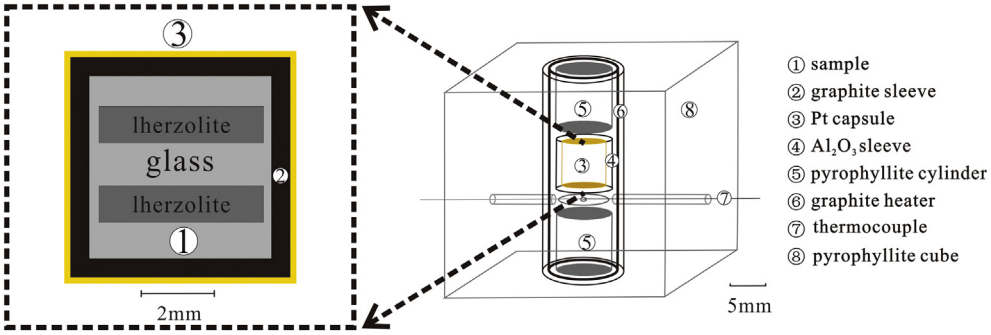

Fig. 2. Sketch map of sample assemblage.

1425 °C and 2 GPa and obtained harzburgite (residual mineral phase composition: Opx + Ol). Wang and Tang (2013) reacted a tonalitic melt with olivine at 1250 °C–1400 °C and 2–5 GPa and obtained high-Mg# magma and harzburgite/lherzolite [residual mineral phase composition: Ol + Opx(r) ± garnet (Grt(r)) ± Cpx(r)]. These studies are important because they confirm that the high Mg# of andesitic melt can be obtained during the melt–peridotite reaction and because they provide the lherzolite solidus in the andesitic melt and lherzolite system.

However, existing experiments have generally been conducted at a particular pressure [e.g., Wang et al., 2010 and Wang et al., 2013 performed experiments at 2 GPa, Rapp et al., 1999 and Rapp et al., 2010 performed experiments at 3.8 GPa, these study can't offer useful information about the effect of reaction P], and the chemical composition of starting melts may not be fully controlled [e.g., the starting melts in Wang et al., 2010 were obtained by the partial melting of eclogite, and the chemical compositions of the melts varied with reaction temperature, similar to those of Yaxley and Green, 1998 and Mallik and Dasgupta, 2012, the reaction P–T in these existing studies is not the unique variable, effect of reaction P–T might be covered by the varied starting melting], the results of such studies cannot adequately answer questions about the relationship between the reaction P–T and the composition of the experimental products. For the present study, we used experiments to create a reaction between tonalitic glass and a lherzolite chip at temperatures of 1250 °C–1400 °C and pressures of 2–4 GPa [below the lherzolite solidus based on existing research (Anderson, 2005; Baker et al., 1995; Gao et al., 2017; Kogiso et al., 2003). The experimental results allow us to investigate the effect of the reaction P–T on the composition of the experimental products. We use the results to explain the compositional differences between Palaeozoic and Mesozoic–Cenozoic mantle xenoliths and the chemical variation in Mesozoic HMAs from the NCC.

2. Study background

The NCC can be divided into three parts (Fig. 1), namely, the Western Block, the Trans-North China Orogen, and the Eastern Block (EB) (Zhao et al., 2001), which amalgamated into a single craton at 1.85 Ga (Wu et al., 2008). The inner EB contains several Palaeozoic diamondiferous kimberlite intrusions with mantle xenoliths (Chi et al., 1996). Based on the mineral inclusions, these xenoliths are believed to have originated from thick (>200 km) and cold (surface heat flow of ~40 mW/m^2) lithospheric mantle. These Palaeozoic mantle xenoliths are refractory (Mg rich) with respect to the major elements and are enriched in Sr–Nd–Hf isotopes (Fan et al., 2000; Menzies et al., 2007; Xu, 2001; Zheng et al., 2005; Zheng et al., 2006). Intensive magmatism occurred during the Mesozoic, and many HMAs formed in the inner NCC. The reaction of silicic melt with mantle peridotite changed the lithospheric mantle of the NCC (Zhang, 2005; Zhang et al., 2007). A large proportion of the mantle xenoliths in Mesozoic–Cenozoic basalts [they were origin from mantle (might be contaminated by silicic melt derived from continental crust) with high Fe/Mn and highly fractionated REE patterns, with plenty of mantle xenoliths (Liu et al., 2005; Liu et al., 2008a)] and Mesozoic HMAs in the inner NCC became enriched in major elements and depleted in Sr–Nd–Hf isotopes as a result of the melt–peridotite reaction. These xenoliths are believed to have originated from thin (~80 km) and hot (surface heat flow of ~80 mW/m^2) lithospheric mantle (Fan et al., 2000; Menzies et al., 2007; Xu, 2001; Zheng et al., 2005; Zheng et al., 2006; Zheng et al., 2016). Two types of reaction vein are found in these Mesozoic–Cenozoic mantle xenoliths: garnet pyroxenite veins (Liu et al., 2005) and pyroxenite veins (Chen and Zhou, 2004; Chen and Zhou, 2005; Xu et al., 2010b). These reaction veins are evidence for the occurrence of melt–peridotite reactions in the lithospheric mantle of the NCC (Liu et al., 2005; Sun et al., 2012; Xiao et al., 2015; Xu et al., 2008; Zheng et al., 2006; Zheng et al., 2007). A small proportion of mantle xenoliths in Mesozoic–Cenozoic basalts have retained their Palaeozoic chemical characteristics, suggesting that they are residuals that escaped the melt–peridotite reaction, with such mantle xenoliths including those found in Hebi and Hanuoba (Yu, 2009). Olivines from Palaeozoic (Pz) refractory mantle xenoliths have higher Forsterite (Fo) contents (≥0.90) compared with olivines from Mesozoic (Mz) and Cenozoic (Kz) enriched mantle (Fo < 0.90) (Zheng et al., 2006). The variation in the Fo content of olivines has been confirmed by many field observations (Chen and Zhou, 2004; Chen and Zhou, 2005; Wang et al., 2012; Xiao et al., 2015; Xu et al., 2008; Xu et al., 2010a; Xu et al., 2010b; Yu, 2009; Zheng et al., 2000).

Table 1
composition of starting material (wt%).

	SiO_2	TiO_2	Al_2O_3	FeO[c]	MnO	MgO	CaO	Na_2O	K_2O	P_2O_5	NiO	Cr_2O_5	Total	Mg#[d]
Tonalite[a]	63.75	0.46	17.45	5.1	0.11	2.82	4.59	4.11	1.4	0.18	N.A.	N.A.	100.00	0.5
Tonalitic glass[a]	63.30	0.45	16.9	5.10	0.12	2.73	4.29	3.79	1.41	0.17	N.A.	N.A.	98.26	0.51
Olivine(50%)[b]	41.30	0.03	0.03	9.74	0.14	49.45	0.05	0.04	0.04	0.01	0.31	0.06	101.22	0.9
Orthopyroxene(22%)[b]	54.46	0.17	4.38	6.30	0.11	33.49	0.63	0.17	0.01	0.18	N.	0.35	100.25	0.91
Clinopyroxene(25%)[b]	52.39	0.54	6.65	2.74	0.07	15.43	19.07	2.05	0.01	0.02	0.03	0.92	99.9014	0.91
Lherzolite[b]	47.75	0.3	4.69	8.24	0.23	27.28	10.15	0.21	0.035	0.037	N.A.	N.A.	99.75	–

Note: a, the data of the tonalite and tonalitic glass are from Wang and Tang (2013); b, the whole-rock chemical composition of mantle Lherzolite and the chemical composition of minerals of this mantle Lherzolite are from Gong et al. (2011); c, FeO = total Fe;d, Mg# = molar (MgO/(MgO + ∑FeO)), N.A. = No analysis.

Table 2
summary of experimental conditions and results.

No.	Temperature (°C)	Pressure (GPa)	Duration (h)	Phase Assemblage
MD-03	1250	3.0	72	Ol + Opx + Gl + Cpx + ***Opx(r)***
MD-04	1300	3.0	48	Ol + Opx + Gl + Cpx + ***Opx(r)***
MD-01	1350	3.0	38	Ol + Opx + Gl + Cpx + ***Opx(r)***
MD-05	1400	3.0	45	Ol + Opx + Gl + Cpx + ***Opx(r)***
TS-07	1350	2.0	72	Ol + Opx + Gl + Cpx + ***Opx(r)***
TS-06	1250	4.0	72	Ol + Opx + Gl + Cpx + ***Opx(r)*** + ***Grt(r)*** + ***Q(r)***
TS-08	1300	4.0	72	Ol + Opx + Gl + Cpx + ***Opx(r)*** + ***Grt(r)***
TS-09	1350	4.0	72	Ol + Opx + Gl + Cpx + ***Opx(r)***
XX-01	1250	4.0	67	Ol + Opx + Gl + Cpx + ***Opx(r)*** + ***Grt(r)*** + ***Q(r)***

Phase abbreviation: Ol = olivine, Gl = melt, Opx = orthopyroxene, Grt = garnet, Cpx = clinopyxene, Q = quartz, ***(r)*** = mineral in reaction rim. The XX-01 is a contrast experiment of TS-06, for checking trace elements' uncertain, its phase assemblage is speculate by microscopic examination.

3. Experimental and analytical methods

The melt–lherzolite reaction experiments in this study were conducted using the DS-3600 six-anvil apparatus at the Key Laboratory for High-Temperature and High-Pressure Study of Earth's Interior at the Institute of Geochemistry of the Chinese Academy of Sciences, Guiyang, China. The experimental pressure was determined via the high-purity bismuth (Bi, threadlet) phase transition pressure at room temperature and the gold (small cylinder) melting pressure at 0.6–6.0 GPa (Fu and Zhu, 1986). The pressure was rechecked using the KCl melting curve according to Tingle et al. (1993) These two independent results showed good agreement. Two types of starting material were loaded (sandwiched) in graphite–platinum double capsules (Fig. 2). The major element compositions of the starting materials are listed in Table 1. The experimental conditions and phase assemblages of the run products are provided in Table 2. The major element contents of the run products are given in Supplementary s-Table 3. The trace element concentrations of the starting materials and reacted melts are listed in Supplementary s-Table 4.

3.1. Starting materials

Tonalite and lherzolite were used as starting materials in this study. Based on previous experimental research (Rapp et al., 1999; Wang et al., 2010; Yaxley and Green, 1998) and geochemical studies of field samples (Gao et al., 2004; Gao et al., 2009), magma derived from delaminated crust is similar to TTG or adakite. Therefore, a tonalitic glass was selected as the starting melt. This glass was processed from a tonalite (sample No. 99SC81) collected from Sandouping in Huangling, Hubei Province, China. The tonalite was crushed into chips, manually ground to a ~200-mesh powder in an agate mortar, melted three times in an Fe-saturated Pt crucible at 1500 °C/1 atm for an hour, and quenched. The glass was then examined with a scanning electron microscope to confirm its homogeneity. The chemical composition of the tonalitic glass is almost the same as that of tonalite (Table 1). The other starting material (a mantle lherzolite xenolith) was collected from the Cenozoic Hannuoba basalt. The olivine in this fresh lherzolite with typical protogranular texture has a high Fo content (up to 0.9) and is very similar to the peridotite of the Palaeozoic mantle reported by Zheng et al. (2006). Therefore, this lherzolite was selected as a starting material to simulate the Palaeozoic mantle. The lherzolite was sawn into chips measuring ~3 mm × 3 mm × 1 mm, and suitable chips (Ol:Opx:Cpx = 2:1:1 volume ratio, maintaining the original lherzolite structure) were selected for the experiment and carefully cleaned in an ultrasonic bath.

3.2. Experimental techniques

The tonalitic glass and lherzolite chips were inserted into graphite-lined Pt capsules (Fig. 2). The capsules were covered with an Al_2O_3 sleeve and placed in the centre of a graphite heater. The top of the assembly was filled with a pyrophyllite cylinder that had been fired at

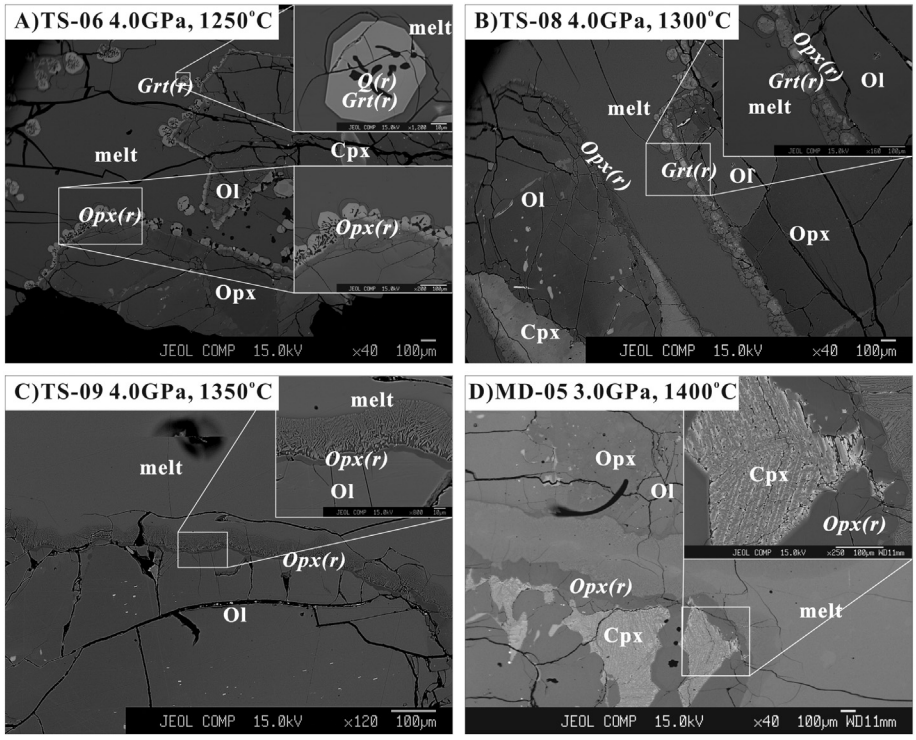

Fig. 3. Representative BSE photos of experiment products. Phase abbreviation: Ol = olivine, Gl = Glass (melt), Opx = orthopyroxene, Grt = garnet, Cpx = clinopyxene, Q = quartz, *(r)* = mineral in reaction rim. There are two kinds of mineral assemblage found in experiment products' reaction rims. The first one is the Opx(r) + Grt(r) ± Q(r), as shown in A&B; another one is the Opx(r), as shown in C&D. In all experiment products, the residual lherzolites were surrounded by the 'new-born' Opx(r).

800 °C. The graphite heating tube was then placed into a pyrophyllite cube (32 mm × 32 mm × 32 mm), which had also been fired at 800 °C. The temperature was measured and controlled via $PtRh_6$–$PtRh_{30}$ thermocouples with an accuracy of ±5 °C. The proportions of the two starting materials in each run were determined based on weight and controlled at a ratio of 1:1 (±0.05). The pressure measurements had an accuracy of ±0.1 GPa (estimated via the variation in the push-cylinder pressure). The oxygen fugacity environment in the experimental runs was approximately FMQ-3 (Tao et al., 2015), which is consistent with the diamond-bearing lithospheric mantle environment. In a single run, the pressure was first raised to the desired value, with the temperature then being increased in three steps to the desired value. These conditions were maintained for the desired duration. The experiment was quenched to <80 °C in 90 s by turning the power off and decompressing. The product of each pre-synthesis run was carefully removed from the capsule and mounted in epoxy and then polished for inspection and electron microprobe analysis.

3.3. Analytical procedures

The chemical compositions of the tonalite and tonalite glass were analysed at the State Key Laboratory of Ore Deposit Geochemistry of

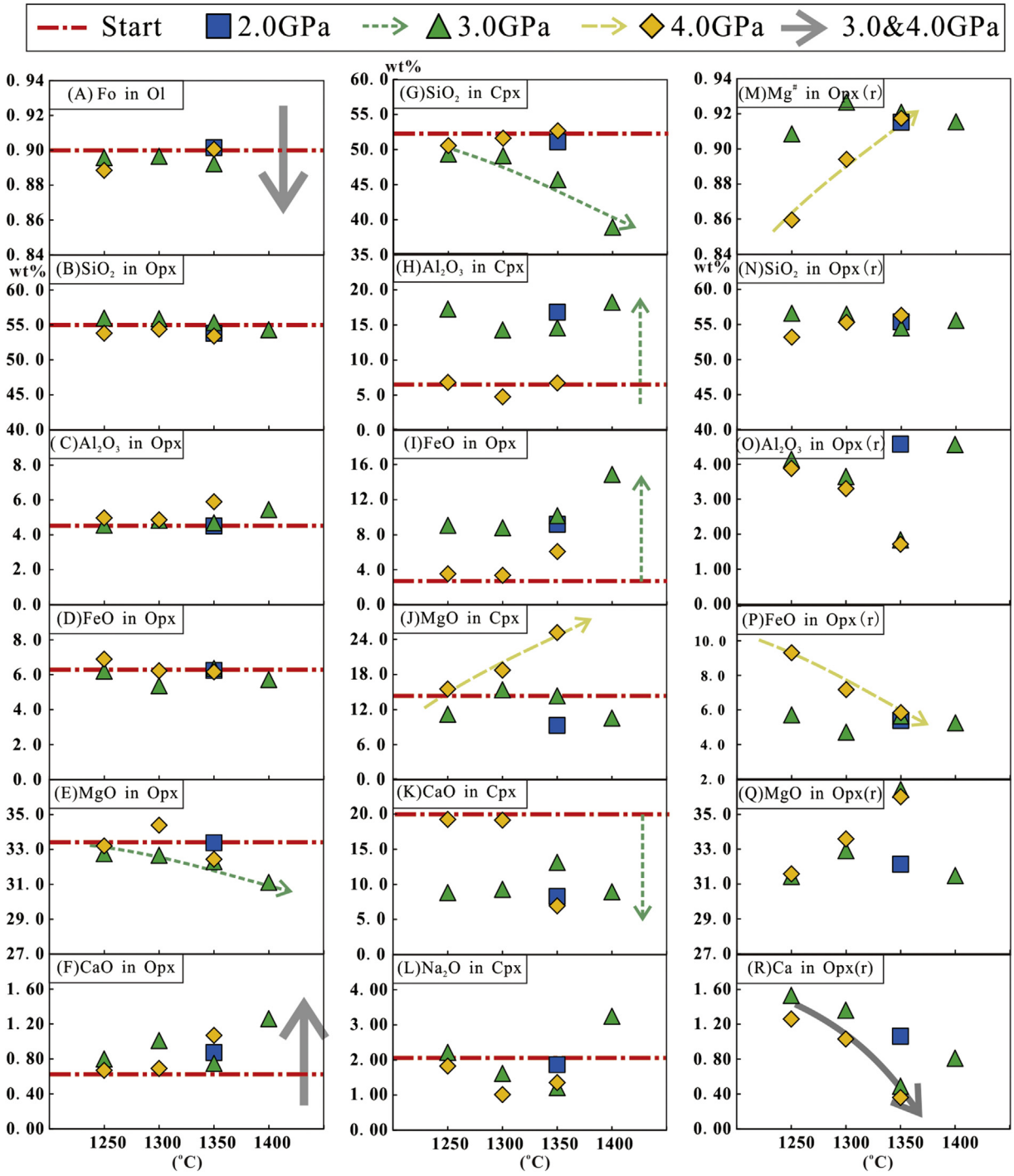

Fig. 4. Plots of Mg# and oxide abundance of minerals in experiment products. Fo = Forsterite contents of olivine; Ol = olivine in residual lherzolite; Opx = orthopyroxene in residual lherzolite; Cpx = clinopyroxene in residual lherzolite; Opx(r) = orthopyroxene in reaction rim. The start value is shown as red line and the arrows mark the variation tendency of oxide contents (or Mg#) with reaction temperature increase.

the Institute of Geochemistry, Chinese Academy of Sciences. The major elements were analysed using an Axios (PW4400) X-ray fluorescence spectrometer. The tonalitic glass trace elements were analysed by inductively coupled plasma mass spectrometry (ICP–MS) following the analytical procedure reported by Qi et al. (2000). The backscattered electron (BSE) images and major element contents of the run products were analysed using a JEOL JXA-8100 electron microprobe at the State Key Laboratory of Isotope Geochemistry, Guangzhou Institute of Geochemistry, Chinese Academy of Sciences. Chemical analyses of the minerals and glass were conducted using a focused beam, 15 kV accelerating voltage, and 10 nA beam current (see Huang et al. (2007b) for details). The trace element compositions of the reacted melts were measured with laser ablation ICP–MS using a GeoLasPro laser ablation system and Agilent 7700× ICP–MS at the Sample Solution Analytical Technology Company. The laser beam size used was 32 μm. Details of the analytical procedures used are reported in Liu et al. (2008b).

4. Results

4.1. Reaction assemblages

The reaction between tonalitic glass and mantle peridotite produced three distinguishable zones: residual peridotite, reaction rims, and a melt pool (Fig. 3). The residual peridotites in the run products have the same compositions as that of the starting lherzolite in the mineral assemblage (Ol + Opx + Cpx). The olivines and orthopyroxenes in the residual peridotites are homogeneous and holistic. Significant change in the structure of Ol/Opx compared with the starting material was not observed. The structure of the clinopyroxene in the residual peridotite changed from holistic to sieve texture in the runs at 3 GPa (Fig. 3D). However, the structure did not change in the samples obtained from the 4 GPa runs. In all run products, the residual peridotite was surrounded by a reaction rim that divides it from the melt pool. As shown in Fig. 3, the reaction rims (veins) can be classified into two types according to their phase assemblage: one contains Opx(r) + Grt(r) ± quartz(r) (Fig. 3A and B), and the other contains Opx(r) only (Fig. 3C and D). The banded and newly formed Opx(r) grains observed in all run products have no characteristic crystal shape. The contacts between the Opx(r) and residual peridotite are distinct (Fig. 3). The width of the banded Opx (r) ranges between 5 and 100 μm and is controlled by the reaction temperature. The width of the banded Opx(r) in the 1250 °C and 3 and 4 GPa run products is approximately 40 ± 10 μm, whereas that of the 1300 °C and 3 and 4 GPa run products is approximately 20 ± 5 μm. The width of the banded Opx(r) is 10 ± 5 μm in the 1350 °C and 2, 3, and 4 GPa runs and ranges from 5 to 150 μm in the 1400 °C and 3 GPa runs. The banded Opx(r) with a width of 150 μm is very nearby Cpx with sieve texture (Fig. 3D). These observations are similar to reports on the reaction of andesitic melt with peridotite (Johnston and Wyllie, 1989; Rapp et al., 1999; Wang et al., 2010; Wang et al., 2013; Wang and Tang, 2013; Yaxley and Green, 1998), suggesting that Opx(r) is widely distributed in similar reactions. In association with Opx(r), Grt(r) grains are usually euhedral and reach sizes of up to 100 μm at 4 GPa and 1250 °C/1300 °C, suggesting that the relatively low T and high P benefit garnet growth, supporting earlier work by Rapp et al. (1999), Johnston and Wyllie (1989), and Yaxley and Green (1998). In run TS-06 (4 GPa, 1250 °C), quartz is found in garnet with a sieve texture (Fig. 3A), similar to the observations of Yaxley and Green (1998). In addition, garnet grains always aggregate and are distributed near the orthopyroxene band and wall of the graphite crucible (Fig. 3A and B). Unitive glasses (melt pools) are observed near the reaction rims in the run products. These glasses have widths of >300 μm (Fig. 3) and are clear and homogeneous, except for several quenched crystals distributed near the reaction rims (Fig. 3C).

4.2. Chemical compositions of run products

The major element contents of all phases (including melt (glass)) of the run products and the trace element compositions of the melt in selected runs are homogeneous within the margin of error (major elements: 3% relative error; trace elements: 10% relative error). A concentration gradient was not determined in our run products, which is very different from the results of dissolution experiments (Morgan et al., 2006; Morgan and Liang, 2005; Wang et al., 2013), indicate that the diffusion process was complete and that an equilibrium was reached. Plots of the Mg# values and oxide abundances of the residual crystalline phases are shown in Fig. 4.

The Fo contents of olivine in residual lherzolite are slightly lower than that of the starting material, except for the 2 GPa / 1350 °C run (Fig. 4A). This result is the same as that obtained in similar melt–peridotite reactions (Wang et al., 2010). The CaO and NiO contents of olivine in residual lherzolite are slightly elevated respect to Ol in starting lherzolite (s-Table 3).

The major element content of orthopyroxene in residual lherzolite does not significantly change during the experimental melt–peridotite

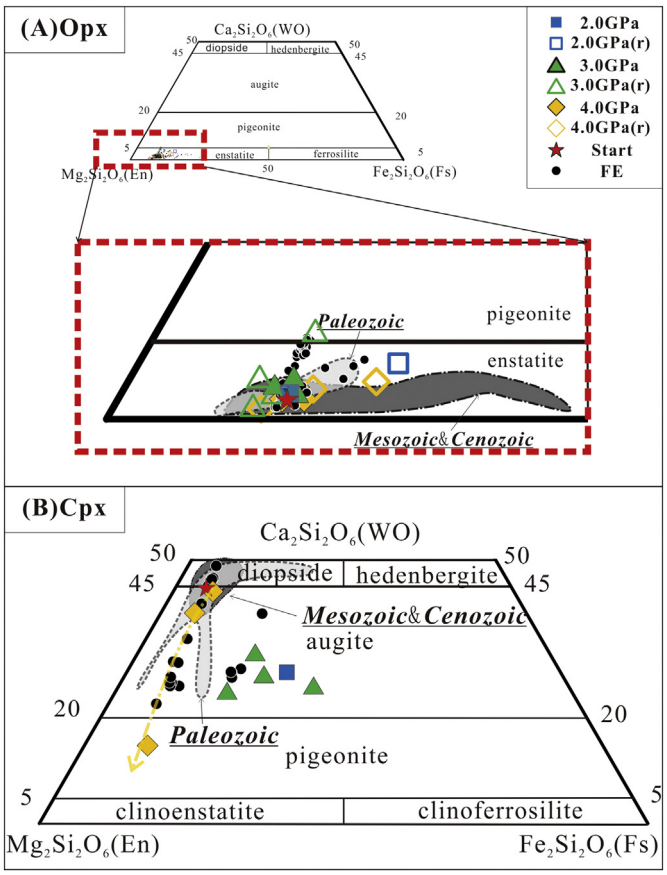

Fig. 5. Composition ranges of pyroxenes in experiment products and NCC's mantle xenoliths. Schematic map of the pyroxenes is refer to Morimoto (1988). Start is the value of Opx/Cpx in starting lherzolite; FE is orthopyroxene(Wang et al., 2010; Wang et al., 2013; Yaxley and Green, 1998) and clinopyroxene (Rapp et al., 1999; Wang et al., 2010; Wang et al., 2013; Yaxley and Green, 1998) in similar melt-peridotite reaction experiment products; (r) means this mineral in reaction rim. Variation range of Orthopyroxene and clinopyroxene in NCC's mantle xenoliths are shown via grey fields, these data (Chen and Zhou, 2004; Chen and Zhou, 2005; Chi et al., 1996; Fan et al., 2000; Sun et al., 2012; Xiao et al., 2010; Xiao et al., 2015; Xu et al., 2008; Xu et al., 2010a; Yu, 2009; Zheng et al., 2005; Zheng et al., 2006; Zheng et al., 2007) include xenoliths located in basalt and kimberlite, along with andesite. The arrows mark the variation tendency of composition ranges with reaction temperature increase.

reaction, except for MgO and CaO. In the 3 GPa runs, the MgO content of the residual Opx linearly decreases with increasing reaction temperature (Fig. 4E). In all runs, the CaO content in Opx is higher than that of the starting lherzolite (Fig. 4F). The SiO_2, Al_2O_3, and FeO contents in the residual Opx are almost the same as those in the starting lherzolite (Fig. 4B, C, and D). The residual Opx is enriched in enstatite (Mg) and depleted in both wollastonite (Ca) and ferrosilite (Fe; Fig. 5A), similar to the Opx in the starting lherzolite and in agreement with the observations of Yaxley and Green (1998), Wang et al. (2010).

The major element content of clinopyroxene in residual lherzolite is affected by the reaction P–T. In the 3 GPa runs, the SiO_2 content of the residual clinopyroxene decreases linearly with increasing reaction temperature (Fig. 4G). The Al_2O_3 and FeO contents are higher and the CaO contents are lower than those of the clinopyroxene in the starting lherzolite (Fig. 4H, I, and K). In the 4 GPa runs, the MgO content increases linearly with increasing reaction temperature (Fig. 4J). The SiO_2, Al_2O_3, FeO, and CaO contents change only slightly compared with those of the starting material, especially in runs conducted at 1250 °C and 1300 °C. The variation in the Na_2O content of the residual Cpx is complex. Cpx always has a lower Na_2O content, except for the run at 1400 °C and 3 GPa (Fig. 4L). The residual Cpx in the 3 GPa runs is enriched in ferrosilite (Fe; Fig. 5B) compared with those at the 4 GPa runs and runs at higher temperatures (>1300 °C), which are enriched in enstatite (Mg). These results agree with those of previous studies (Rapp et al., 1999; Rapp et al., 2010; Wang et al., 2010; Wang et al., 2013; Yaxley and Green, 1998).

Orthopyroxene in the reaction rims is also enriched in enstatite (Mg) and depleted in wollastonite (Ca) and ferrosilite (Fe; Fig. 5A). However, the amplitude of the Opx(r) variation is higher than that of the residual orthopyroxene. The CaO content decreases linearly with increasing reaction temperature (Fig. 4R). In the 3 GPa runs, the reacted orthopyroxene is depleted in FeO (Fig. 4P) and has a very high Mg# (Fig. 4M). In contrast, the FeO content decreases with increasing reaction temperature in the 4 GPa runs such that the Mg# increases with increasing reaction temperature (Fig. 4M and P).

In addition to the chemical composition of the crystalline assemblage, the composition of the residual glass (melt) changes during the experimental melt–peridotite reaction. Fig. 6 shows that the reacted melt coexisting with the crystalline assemblage contains 55–68 wt% SiO_2. The MgO and CaO contents and Mg# are higher than those of the starting tonalite, whereas the Na_2O and K_2O contents are lower than those of the starting tonalite. In the 3 GPa runs, the SiO_2, Al_2O_3, and CaO contents decrease linearly with increasing reaction temperature (Fig. 6A, B, and E). The residual melt has a higher MgO concentration and Mg# and lower Na_2O content than does the starting tonalitic glass (Fig. 6D, H, and F). In the 4 GPa runs, the SiO_2, Al_2O_3, and K_2O concentrations decrease linearly with increasing reaction temperature, whereas the FeO, MgO, and Na_2O contents and Mg# show the opposite trend.

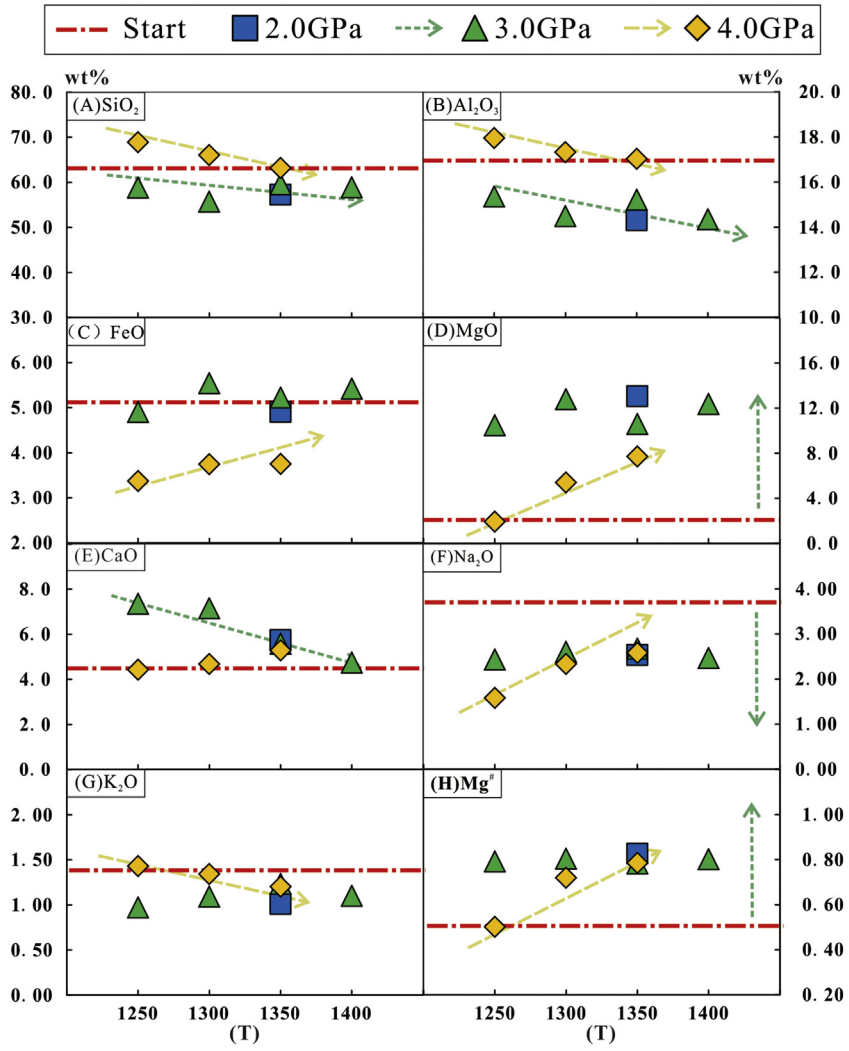

Fig. 6. Plots of Mg# and oxide abundance of reacted melt. The start value is shown via red line and the arrows mark the variation tendency of oxide contents and Mg# with reaction temperature increase.

The major element variation of the reacted melt is similar to that of other melt–peridotite reaction products, with many studies having confirmed that the Mg# of the reacted melt increases sharply after a melt–peridotite reaction (Gao et al., 2017; Rapp et al., 1999; Sekine and Wyllie, 1982; Shaw and Dingwell, 2007; Wang et al., 2010; Wang et al., 2013; Wang et al., 2016; Wang and Tang, 2013; Yaxley and Green, 1998). The major element variation of the 4 GPa runs is similar to that reported by Rapp et al. (1999) and Wang and Tang (2013).

We also investigated the trace element contents of the reacted melts. A primitive-mantle-normalized spider diagram and chondrite-normalized rare earth element (REE) curve were drawn to interpret the trace element concentrations of the residual melts (Fig. 7). In the spider diagram, most of the elements of the residual melt of selected runs follow the pattern of the starting glass, except for Nb. In addition, the Y–Lu concentrations in run TS-06 show a different trend from that of other runs, and the starting glass was most probably affected by the large-scale crystallization of garnet (Table 2 and Fig. 3A). These results are supported by the REE curves (Fig. 7B). Sample TS-06 is depleted in heavy rare earth elements (HREEs, Gd–Lu), whereas the other two runs show almost the same distribution pattern as starting tonalitic glass. The Nb in reacted melt (TS-06/07/08) is strange, and then a contrast experiment was conducted on a Piston Cylinder Press at Suzhou University, Anhui, China. The pt./graphite capsule (2.5 mm inner) was used, the manmade lherzolite powder (Ol: Opx: Cpx = 2: 1: 1 in weight) was reacted with the tonalitic glass, trace element of reacted melt was analysis using the same method at the same company; the result is listed in s-Table 4. The Nb and Ta (and Cu/Ag/Sn) of reacted melt (TS-06) are abnormal for unknown reason, the TS-07 and TS-08 may have the same problem. However, most of trace element in TS-06 and XX-1 show good consistency, and should be credible.

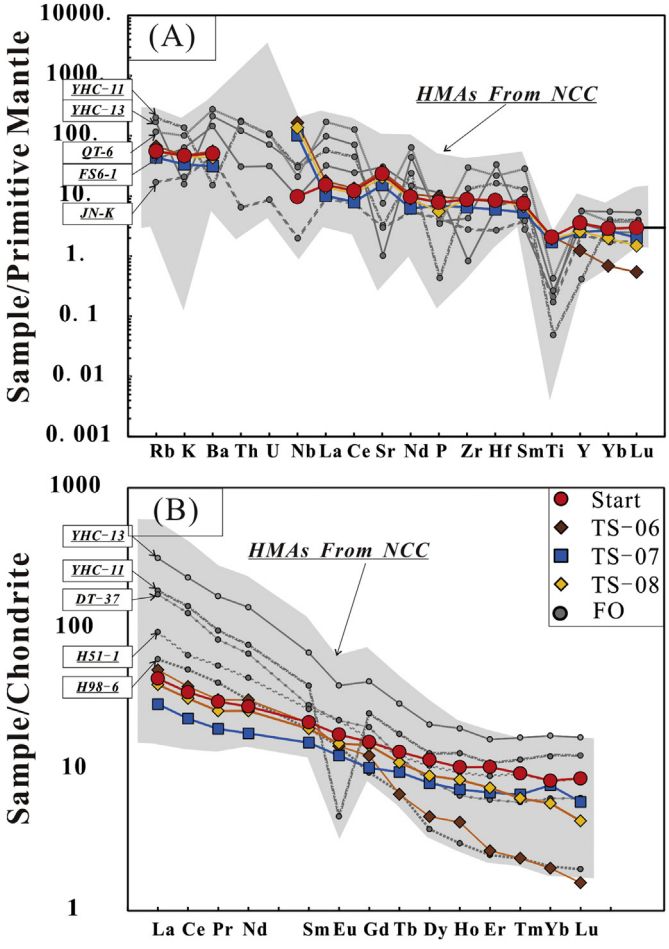

Fig. 7. Primitive mantle normalized spidergram and chondrite-normalized rare earth element abundance patterns of experimental melt and filed observed rocks. TS-06/07/08 runs reported in this paper, their run details could refer to Table 2; Start, the value of start tonalite; FO, field observed Mesozoic high Mg# andesitic rocks (Chen et al., 2013; Ma et al., 2016; Wang et al., 2006; Wu et al., 2003; Xu et al., 2006a; Xu et al., 2006b; Xu et al., 2009a; Xu et al., 2010b; Yang, 2007; Yuan et al., 2006; Zhang et al., 2003a; Zhang et al., 2003b; Zi et al., 2007), their variation range are shown in grey fields, representative samples are shown with lines and their sample numbers are listed in boxes on the Y axis. DT-27, YHC-11 and YHC-13 are from Yuan et al. (2006); H51–1 and H98–6 are from Xu et al. (2006b); JN-K and QT-6 are from Yang (2007); FS6–1 is from Xu et al. (2010b). Data of primitive mantle and chondrite for normalizing are from Sun and McDonough (1989).

5. Discussion

5.1. Formation of different reaction veins in xenoliths

Two types of reaction vein form in mantle xenoliths in Mesozoic–Cenozoic magma in the inner NCC (garnet pyroxenite veins and pyroxenite veins). These veins constitute key evidence regarding the reaction of silicate melt with peridotite in the Mesozoic lithospheric mantle of the NCC. However, the following important questions remain unanswered: 1) How were the veins generated? 2) Why are there two different types of vein? We answer these questions below.

1) The melt–peridotite reaction is responsible for the generation of the veins. However, not every reaction between silicic melt and peridotite causes a reaction vein. Based on experimental results (including those from this study), there are at least three types of reaction between silicic melt and peridotite: dissolution, complete equilibrium reactions, and local equilibrium reactions. Dissolution is usually observed in experiments with short run times (<8 h) (Morgan et al., 2006; Morgan and Liang, 2003, 2005; Wang et al., 2013; Wang et al., 2016); minerals (Cpx or Cpx + Opx) with low melting points will disappear from the reaction rims, and reaction veins do not form. Complete equilibrium reactions are often observed in experiments with long run times (>24 h) and involving a high proportion of melt (or filling used mixture powder or a high proportion of water) (Johnston and Wyllie, 1989; Rapp et al., 1999; Rapp et al., 2010). The reaction minerals crystallize and form residuals without olivine (Grt ± Opx ± Cpx). However, it is observed that most xenoliths in Mesozoic–Cenozoic magma in the inner NCC contain olivines. Local equilibrium reactions are usually observed in experiments with long run times (>24 h) in layers filling manner (Wang et al., 2010; Wang and Tang, 2013; Yaxley and Green, 1998). In such experiments, reaction veins were found with reacted melt residuals in almost every run. Thus, local equilibrium is the mechanism by which veins could have been formed in Mesozoic lithospheric mantle in the inner NCC.
2) By comparing the experimental results reported in the present study with the mineral compositions of the reaction veins of xenoliths in Mesozoic igneous rocks from the inner NCC, the reason for the occurrence of different types of reaction vein can be clarified. Fig. 8A and B show that the mineral compositions of the reaction rims in experiment run TS-08 are very similar to those of the reaction veins in the DMP-24 mantle xenoliths reported by Liu et al. (2005). Fig. 8C and D shows that the mineral compositions of the reaction rims in experiment run MD-04 are very similar to those of the reaction veins in FS6–59 mantle xenoliths reported by Xu et al. (2010b). The perfect match between experimental products and veins in field xenoliths indicates that they were generated by very similar processes, suggesting that silicic melt–peridotite reactions occurred in the lithospheric mantle in the inner NCC during the Mesozoic. The mineral assemblages of the reaction veins depend on the P–T of the melt–peridotite reaction. The possible boundary of Opx (r) and Opx(r) + Grt(r) is shown in Fig. 8E. Relatively high P and low T benefit the generation of Opx(r) + Grt(r) veins, whereas

Opx veins are generated in relative low P and high T. The reaction vein mineral assemblage was determined via the following empirical discriminant function:

$Y = 3.33 \times 10^{-6} T^2 - 2.17 \times 10^{-3} T - 0.5 - P.$

(T in °C, P in GPa; Y ≥ 0: Opx veins form; Y < 0: Opx + Grt veins form).

5.2. Variation in the mineral chemical composition of xenoliths from the NCC

The interaction between tonalitic melt and peridotite produces two types of reaction vein in mantle peridotite. This melt–peridotite reaction is also responsible for changes in the chemical compositions of lithospheric mantle minerals, as confirmed by studies of xenoliths in Mesozoic and Cenozoic igneous rocks from the inner NCC (Chen and Zhou, 2004; Chen and Zhou, 2005; Xu et al., 2010b; Zhang et al., 2007). To investigate the effect of the reaction P–T on the variation in the chemical composition (major elements) of mantle minerals during melt–peridotite interaction, we compared three minerals (Ol, Opx, and Cpx) in mantle xenoliths in Palaeozoic rocks with those in Mesozoic and Cenozoic rocks (Fig. 9).

5.2.1. Olivine

The Fo content of olivine is the most sensitive and effective index for distinguishing the source of xenoliths. The Fo content of olivine is higher in Palaeozoic mantle xenoliths (Fo ≥ 0.90) than in Mesozoic and Cenozoic mantle xenoliths (Fo ≤ 0.90) (Zheng et al., 2006). This variation is also observed in all experimental products (Figs. 4A and 9A–D). In addition to the decreasing Fo content during the experimental melt–peridotite reaction, the SiO_2 content of residual olivines in experimental products also decreases and its range of variation matches that observed in Mz and Kz mantle olivine (Fig. 9A). The SiO_2 content of olivines in 4 GPa runs decreases more than it does at lower pressure runs. MnO content increases with decreasing Fo content in Mz and Kz mantle xenoliths inner NCC (Yu, 2009; Zheng et al., 2000) but does not do so in Pz mantle xenoliths. The difference in the MnO content of olivine between Pz mantle xenoliths and Mz and Kz mantle xenoliths is consistent with the results of the 4 GPa runs (Fig. 9B). The CaO content of synthetic olivine from the experiments reported in the present study is very similar to that of olivine found in NCC mantle xenoliths and much lower than that reported in similar experimental studies (Wang et al., 2010; Wang et al., 2013). Based on our 4 GPa experiment, the CaO content increases slightly during the melt–peridotite reaction, which is consistent with field observations (Fig. 9C), and the NiO content of olivine also increases. These results agree with that obtained for samples obtained from Xi'anli (Xu et al., 2010a). In the 3 GPa runs, the NiO content decreases slightly during the reaction, whereas the variation based on field observations of xenoliths in Mz and Kz samples is wider (Fig. 9D), indicating that the olivine in these xenoliths reacted with silicic melt at varied depths.

5.2.2. Orthopyroxene

Orthopyroxene in mantle xenoliths can be classified into two types based on the morphology of field samples, namely, macro-grained Opx and vein Opx, corresponding to residual Opx and reaction Opx (r) in experimental products, respectively. The Mg# is an important index for the classification of xenolith groups (Wang et al., 2013). The oxide content of orthopyroxene is plotted versus the Mg# of orthopyroxene in Fig. 9E–9J. Compared with Pz xenoliths, Mz and Kz orthopyroxenes show a wider variation in oxide content and Mg#, whereas most of the Mz and Kz macro-grained Opx samples match the residual samples in the run products. Mz and Kz Opxs' TiO_2 and CaO contents increase slightly during the reaction and the Al_2O_3, MnO, and Cr_2O_3 contents are almost the same as those of Pz Opx. Although the Mz and Kz vein Opx have a wider compositional range than that of residual, their composition depends on the reaction P and T. The Opx(r) in the 3 GPa runs have higher Mg# and CaO contents and lower NiO contents than do those in the 4 GPa runs. Some Mz and Kz macro-grained Opx have a wider compositional range (Fig. 9), with their chemical compositions being very similar to those of vein Opx in the field and reaction Opx(r) in the experiments. These macro-grained Opx might have been generated as vein Opx and subsequently lost their morphology. Although showing very wide compositional variation, orthopyroxene in NCC mantle xenoliths is enstatite (Yu, 2009), which agrees with the experimental results (Fig. 5A).

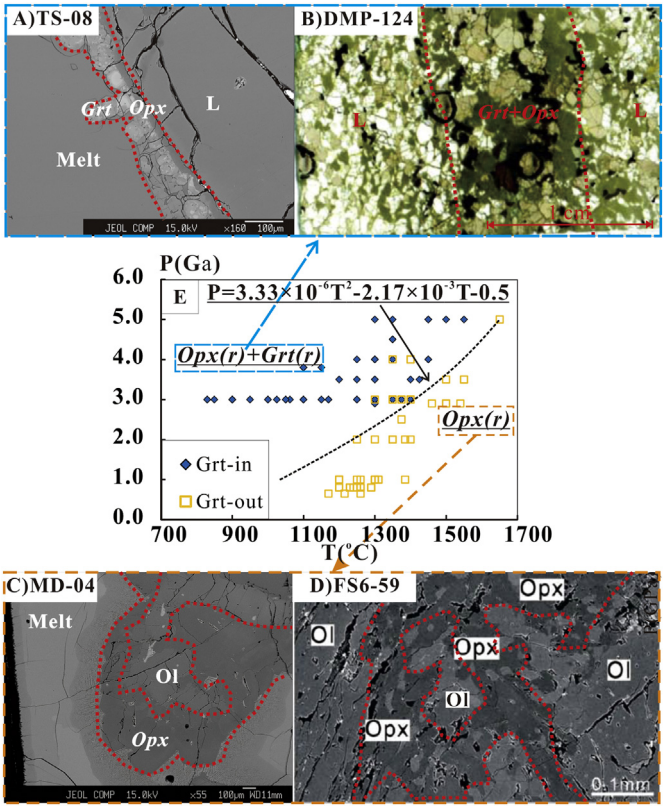

Fig. 8. Minerals assemblage of reacted veins in the reaction between intermediate magma and mantle peridotite based on laboratory experiments and field observation. Phase abbreviation: Ol = olivine, Opx = orthopyroxene, Grt = garnet, L = lherzolite, Grt-in, Garnet present in run product; Grt-out, Garnet disappear in run product. Inclined letter abbreviation means the mineral generated in melt-lherzolite reaction. A&C are BES photos of experimental products in this study, B is a photo of section-scale garnet pyroxenite veins in lherzolites from Liu's Fig. 4C(Liu et al., 2005), D is a BSE photo of a pyroxenite vein from Xu's Fig. 2h (Xu et al., 2010b). The experiment products and the veins founded in mantle xenoliths inner NCC match well. E is the boundary of the two kinds of reaction veins on the reaction thermobaric diagram which is offered via statistical analysis of existing experimental results (Bleeken et al., 2011; Gao et al., 2017; Johnston and Wyllie, 1989; Kelemen et al., 1998; Mallik and Dasgupta, 2012; Rapp et al., 1999; Rapp et al., 2010; Sekine and Wyllie, 1982; Tursack and Liang, 2012; Wang et al., 2010; Wang et al., 2013; Wang et al., 2016; Wang and Tang, 2013; Yaxley and Green, 1998) and our experimental data, the empirical formula is given by Office Excel 2010.

5.2.3. Clinopyroxene

Clinopyroxene is rare in NCC mantle xenoliths compared with olivine and orthopyroxene but is important for the affirmation of the reaction conditions (Zheng et al., 2000). The Mg# of clinopyroxene in mantle Mz and Kz xenoliths ranges mainly from 0.88 to 0.95, which matches that of the samples of the 4 GPa runs. The Pz, Mz, and Kz clinopyroxenes show similar variations in their TiO_2, MnO, Na_2O, and Cr_2O_3 contents (Fig. 9K–9P). However, Mz and Kz clinopyroxenes are slightly enriched in CaO and Al_2O_3 compared with Pz clinopyroxene. Compared with the

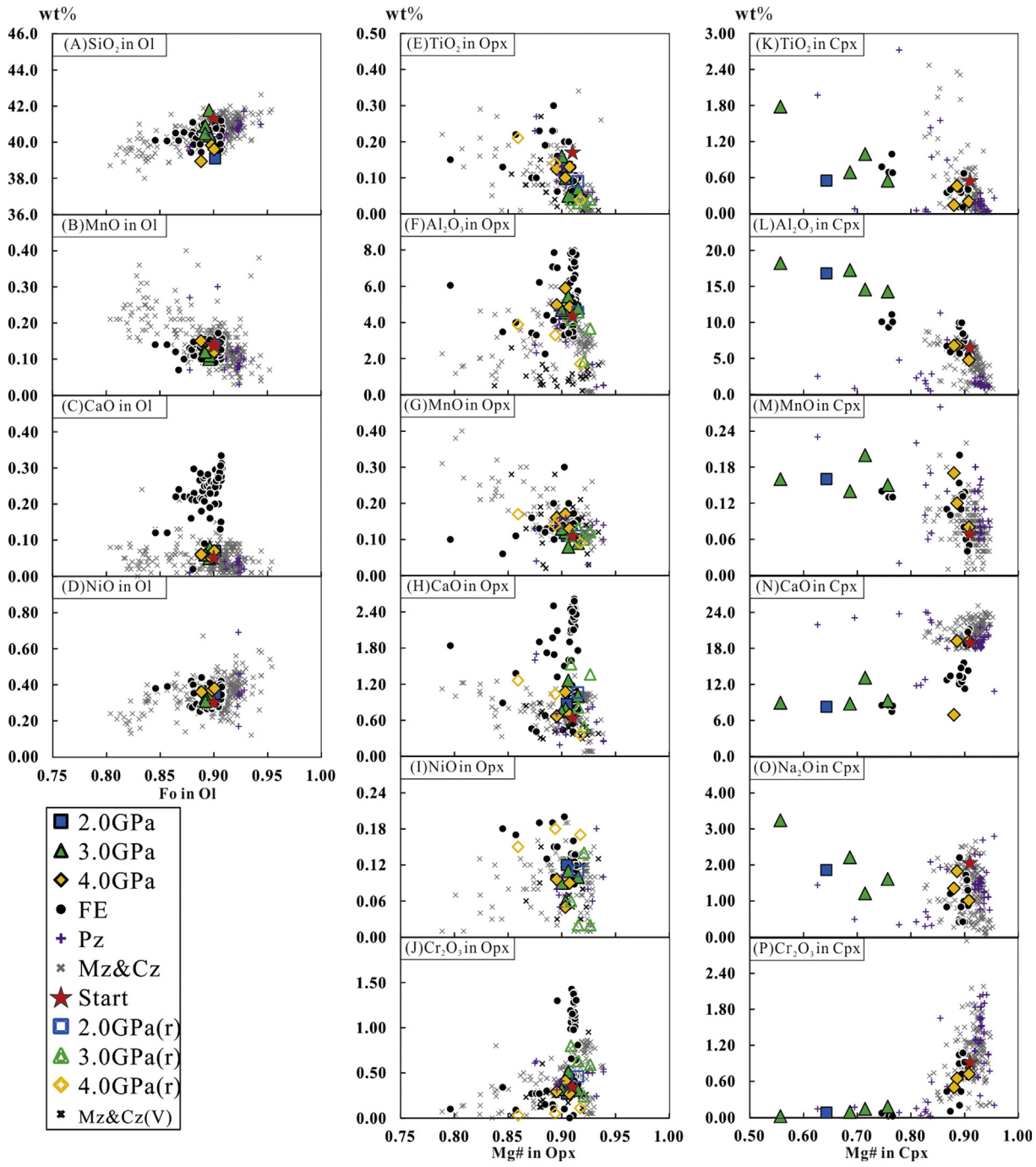

Fig. 9. Variations of oxide abundances versus Mg# (Fo) of minerals in experiments and those from field observations in the NCC. Phase abbreviation: Ol = olivine, Opx = orthopyroxene, Cpx = clinopyroxene. Start, start value in starting lherzolite; 2.0GPa/3.0GPa/4.0GPa, data of this study; 2.0GPa(r)/3.0GPa(r)/4.0GPa(r), orthopyroxene in reaction rims; FE, data of existing experiment results(Rapp et al., 1999; Wang et al., 2010; Wang et al., 2013; Yaxley and Green, 1998); Pz, data of olivine/orthopyroxene/clinopyroxene in NCC's Palaeozoic mantle xenoliths(Chi et al., 1996; Xiao et al., 2010; Zheng et al., 2000; Zheng et al., 2005; Zheng et al., 2006; Zheng et al., 2007); Mz&Cz, data of olivine/orthopyroxene/clinopyroxene in NCC's Mesozoic and Cenozoic mantle xenoliths(Chen and Zhou, 2004; Chen and Zhou, 2005; Fan et al., 2000; Sun et al., 2012; Wang et al., 2012; Xiao et al., 2010; Xiao et al., 2015; Xu et al., 2008; Xu et al., 2010a; Yu, 2009; Zheng et al., 2005; Zheng et al., 2006; Zheng et al., 2007); Mz&Cz (V), orthopyroxene in veins found in NCC's Mesozoic and Cenozoic mantle xenoliths(Chen and Zhou, 2004; Chen and Zhou, 2005; Xu et al., 2008).

experimental result, the residual clinopyroxene in the 4 GPa runs matches the Mz and Kz clinopyroxenes with respect to the variation in oxide contents, except for CaO. The residual clinopyroxene in run TS-09 has a lower CaO content (Fig. 9N). This indicates that the xenoliths containing clinopyroxenes were generated at depths of >130 km and at a temperature of ~1300 °C. This conclusion is also supported by the morphology of the clinopyroxenes. Residual clinopyroxene of the 3 GPa runs has a sieve texture (Fig. 3D), whereas residual macro-grained Cpx (similar to that in NCC mantle xenoliths) was found in the 4 GPa runs. The clinopyroxene in mantle xenoliths is mainly diopside with lower Fs contents (Chen and Zhou, 2004; Chen and Zhou, 2005; Wang et al., 2012). This clinopyroxene matches the residual clinopyroxene of the 4 GPa runs, whereas the crystals in the 2 and 3 GPa runs have higher Fs contents (Fig. 5B). The residual clinopyroxene in the 4 GPa runs also

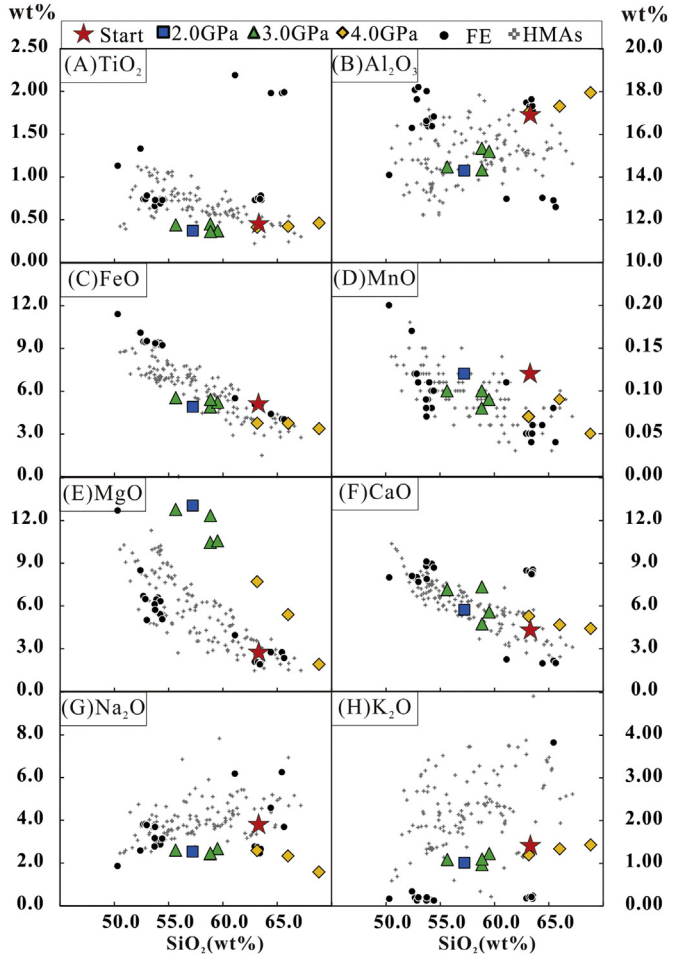

Fig. 10. Harker diagrams of residual melt in experiment products and NCC's Mesozoic HMAs. Start, start value in starting tonalitic glass; 2.0GPa/3.0GPa/4.0GPa, data of this study; FE, existing experimental results (Rapp et al., 1999; Wang et al., 2010; Wang and Tang, 2013); HMAs, Mesozoic High Mg# andesite located inner NCC (Gao et al., 2004; Huang et al., 2007a; Ma et al., 2016; Wu et al., 2003; Xu et al., 2006a; Xu et al., 2006b; Xu et al., 2008; Yang, 2007; Yuan et al., 2006; Zhang et al., 2003a; Zhang et al., 2003b; Zi et al., 2007).

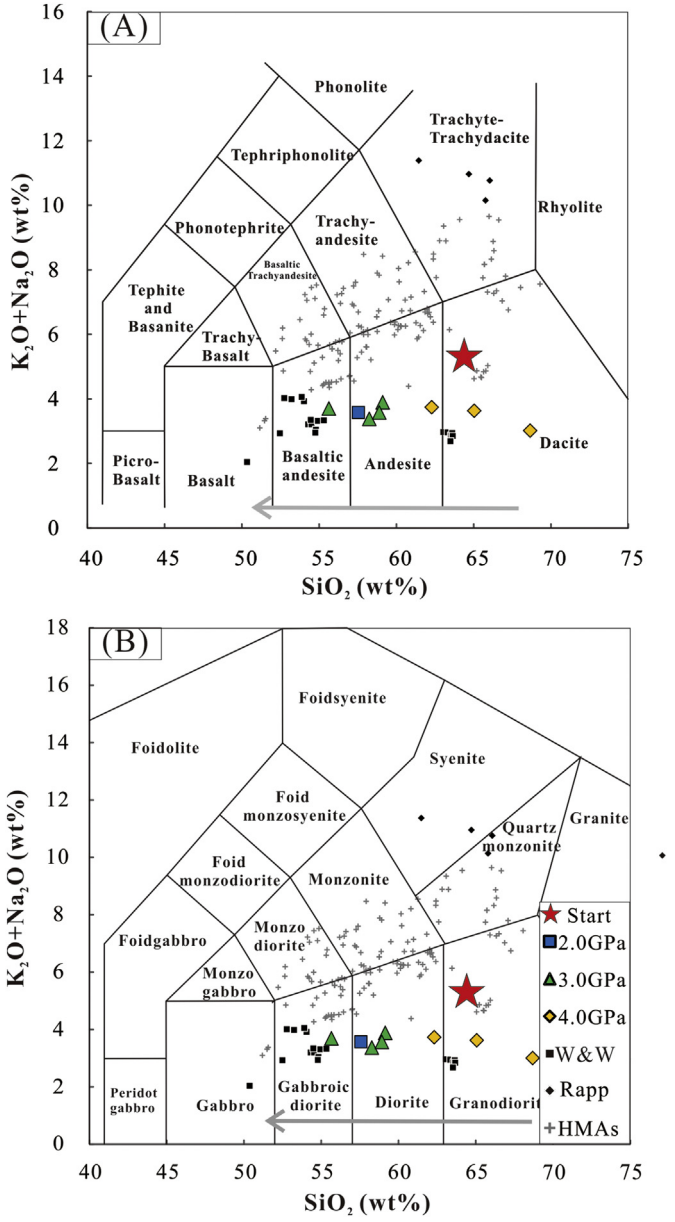

Fig. 11. Total alkali versus silica (TAS) variation diagram. Fig. A is after Maitre (1989) and Fig. B is after Middlemost (1994). Start, start value in starting tonalitic glass; 2.0GPa/3.0GPa/4.0GPa, data of this study; W&W, experiment results from Wang et al. (2010) and Wang et al. (2013), their $Na_2O + K_2O$ content in starting melt is 2.38–3.12 wt%; Rapp, experiment result from Rapp et al. (1999), their $Na_2O + K_2O$ content in starting melt is 8.24 wt%. HMAs, Mesozoic High Mg# andesite located inner NCC (Gao et al., 2004; Huang et al., 2007a; Ma et al., 2016; Wu et al., 2003; Xu et al., 2006a; Xu et al., 2006b; Xu et al., 2008; Yang, 2007; Yuan et al., 2006; Zhang et al., 2003a; Zhang et al., 2003b; Zi et al., 2007). The light grey marks the variation tendency of SiO_2 as reaction temperature rising.

shows a general compositional trend, characterised by diopside being formed under lower reaction temperatures and augite, pigeonite, or clinoenstatite being formed as the temperature is increased (Fig. 5B).

Based on the above discussion, the effect of the melt–peridotite reaction P–T on the mineral composition of the mantle can be clarified, and the results can be used to classify the source of mantle xenoliths and understand the causes of lithospheric mantle evolution. Compared with xenoliths (reacted with intermediate melt) sourced from a depth of ~130 km (equal to 4 GPa), xenoliths (reacted with intermediate melt) from a depth of ~100 km (equal to 3 GPa) contain (1) olivines with higher SiO_2 and lower NiO and MnO contents and (2) orthopyroxenes with higher Mg#, higher CaO contents, and lower NiO contents. The xenoliths (reacted with intermediate melt) containing clinopyroxene might have originated from cold (<1300 °C) and deep lithospheric (~135 km) mantle.

5.3. HMA generation in the NCC during the Mesozoic

As discussed above, the reaction of andesitic melt with peridotite leads to the formation of reaction veins and residual minerals with various chemical compositions. The melt composition also varies during this reaction. The most characteristic trend is that intermediate magma achieves a high Mg#, as found for Mesozoic HMAs from the inner NCC. To determine why the chemical composition of HMAs varies, we compared experimental reacted melt with NCC Mesozoic HMAs using Harker diagrams (Fig. 10). The major elements of the reacted melt in the Harker diagrams show a continuous change depending on variation in the reaction P and T. Reacted melt of the 4 GPa runs has a higher SiO_2 content than that of the 2 and 3 GPa runs, and the SiO_2 content decreases with increasing reaction temperature (Figs. 6A and 10). The variation in the FeO, Al_2O_3, MnO, and CaO contents of the experimentally reacted melts is the same as that in those of the Mesozoic NCC HMAs, whereas the residual melt reported in this study has higher MgO contents and lower TiO_2, Na_2O, and K_2O contents. The Na_2O and

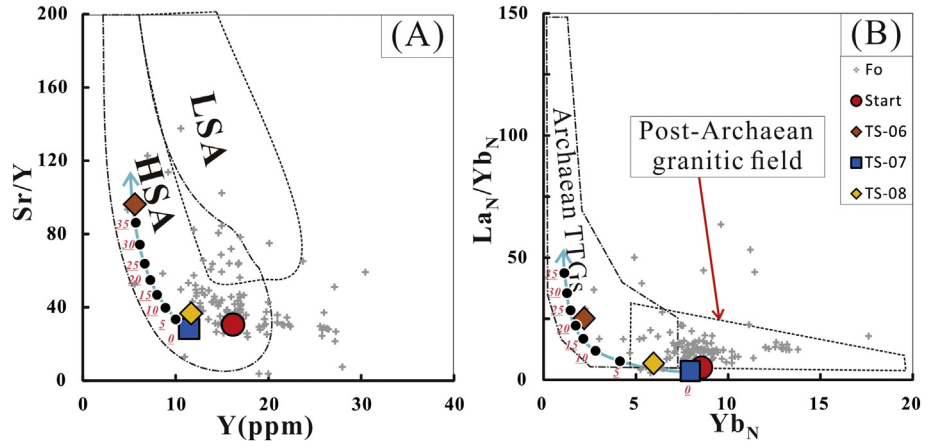

Fig. 12. Plots of Sr/Y vs Y (A) (after(Martin et al., 2005)) and LaN/YbN vs YbN (B) (after Martin (1986)). Start, start value in starting tonalitic glass; 2.0GPa/3.0GPa/4.0GPa, data of this study; HMAs, Mesozoic High Mg# andesite located inner NCC (Gao et al., 2004; Huang et al., 2007a; Ma et al., 2016; Wu et al., 2003; Xu et al., 2006a; Xu et al., 2006b; Xu et al., 2008; Yang, 2007; Yuan et al., 2006; Zhang et al., 2003a; Zhang et al., 2003b; Zi et al., 2007). The light blue arrows show the computation according distribution coefficient from Rapp et al. (2010), the red number show the relative amount of garnet and melt. (TS-07 is chosen as the starting melt, $D_{Grt\text{-}Melt}$ of Sr/Y/La/Yb = 0.0031/10.085/0.0019/19.826, Grt:Melt = X:1-X).

K_2O contents depend on the starting melt, with both being extremely depleted in the starting lherzolite (Table 1). During the reaction, parts of the lherzolite dissolve into the melt, and the Na_2O is replenished based on the clinopyroxene destruction, but K_2O is not supplemented. Subsequently, the reaction vein is formed, with K being more incompatible than Na. Less K_2O is lost during vein generation, and therefore the Na_2O/K_2O ratio of the residual melt (~2.5) shows no significant increase compared with that of the starting glass (~2.9). The Na_2O/K_2O ratio is also affected by the starting melt. The TiO_2 content is very similar to the Na_2O and K_2O contents. The TiO_2 content of the residual melt is almost invariably compared with that of the starting tonalite (Fig. 10A), whereas the higher MgO content of the residual melt needs to be eliminated by further processing. The classifications for the reacted melt and Mesozoic HMAs from the NCC are compared in Fig. 11. The reaction P and T control the SiO_2 content, and the parental magma controls the $Na_2O + K_2O$ content, as discussed above. These two factors are responsible for the marked differences in the major element composition of the Mesozoic HMAs compared with the NCC.

In addition to the major elements, the trace elements were also investigated to understand and explain the trace element variation in Mesozoic NCC HMAs. Fig. 7 shows that most trace elements of the reacted melt are affected mainly by the starting glass. The trace element contents decrease slightly during the melt–peridotite reaction because of the 'dilution effect', and the partition curves are almost the same as that of the starting material. However, the HREEs are controlled by the intense crystallization of garnet (such as in run TS-06) in the reaction rim. These elements decrease with the amount of garnet crystallization and are controlled by the reaction P–T, as discussed above. Similar to the HMAs studied by Hutouya and Tiezhai (Xu et al., 2006b), the REE abundance patterns are very similar to that of the residual melt in run TS-06, with large-scale garnet crystallization. The Sr/Y–Y and La_N/Yb_N–Yb_N diagrams are effective in classifying whether a magma is adakite (or TTG). The Sr/Y–Y and La_N/Yb_N–Yb_N characteristics of the melt are also controlled by the crystallization of garnet and indirectly controlled by P and T. The Sr content of Mesozoic HMAs was most likely inherited from the parental magma and was less affected by the crystallization of garnet. In our experiments, Y content decreased during the garnet crystallization reaction, enhancing the Sr/Y ratio in run TS-06 (Fig. 12A). The La and Yb contents of HMAs are also controlled by the crystallization of garnet. The geochemical behaviour of La is similar to that of Sr, whereas the behaviour of Yb is similar to that of Y. The melt enhances the La_N/Yb_N ratio compared with the parental magma when garnets crystallize during the reaction (such as TS-06) or vice versa (such as TS-07). Based on the distribution coefficient reported by Rapp et al. (2010), the content of crystalline garnet can be used to estimate the generation of adakite (or TTG) magma. A garnet crystal content of ~15%–20% in intermediate magma leads to adakite-like magma. This estimate was verified with the TS-06 and TS-08 runs, which had garnet contents of 25%–35% and < 5%, respectively, compared with the residual melt. This result is compatible with the BSE photos of experimental products in Fig. 3. Adakite-like HMAs generation during melt-peridotite reactions inner NCC is similar to the generation process of high Si adakites(HSA), which is believed to represent subducted slab-melts that have reacted with peridotite during ascent through mantle wedge (Martin et al., 2005), so most of adakite-like HMAs plot in HSA filed in Fig. 12A.

6. Conclusions

The effect of reaction pressure (P)and temperature (T)on the melt–peridotite reaction was investigated via reaction experiments between tonalitic melt and mantle lherzolite at pressures of 2–4 GPa and temperatures of 1250 °C–1400 °C. Combining our results with those of previous melt–peridotite reaction experiments, the following conclusions regarding the compositional changes of Mesozoic and Cenozoic mantle xenoliths and the variation in the chemical composition of Mesozoic high-Mg# andesites (HMAs) from the North China Craton (NCC) can be made:

1. Reaction veins in xenoliths in Mesozoic magma from the NCC were generated by local equilibrium reactions between intermediate magma and mantle peridotite. The mineral assemblages are controlled by the reaction P and T and can be determined via the empirical discriminant function: $Y = 3.33 \times 10^{-6} T^2 - 2.17 \times 10^{-3} T - 0.5 - P$ (T in °C, P in GPa; Y ≥ 0: Opx veins form; Y < 0: Opx + Grt veins form).
2. The andesitic melt–peridotite reaction changes the major element compositions of the main mantle minerals (olivine, orthopyroxene, and clinopyroxene). This change is similar to the difference between Palaeozoic refractory lithospheric mantle and Mesozoic–Cenozoic fertile mantle. The compositional change/difference is affected by the reaction P and T. The reacted-mantle xenoliths from deeper lithospheric mantle contain olivines that are depleted in SiO_2 and enriched in NiO/MnO and lower-Mg# orthopyroxenes that are enriched in NiO and depleted in CaO. Clinopyroxene-bearing xenoliths are formed only during high-P and low-T reactions (4 GPa, ≤1300 °C).
3. The NCC HMAs were generated as a result of melt–peridotite reaction. The SiO_2 content of the reacted melt is controlled by the reaction P and T. An increasing reaction P increases the SiO_2 content, and an increasing reaction T reduces the SiO_2 content. The Na_2O and K_2O

contents of the reacted melt are controlled by the parental magma, but the Na_2O/K_2O ratio changes little during the reaction. Most of the trace elements in the reacted melt are diluted, and their contents decrease. However, the partition curve follows that of the parental magma, except for HREEs, which are controlled by the intense crystallization of garnet. Magmas generated from few or no garnet residual reactions follow the REE partition curve of the parental magma, whereas the magma obtained from the garnet residual reaction has a right-deviated chondrite-normalized REE partition curve. A total of 15%–20% garnet crystallization from intermediate magma gives the residual melt adakite-like properties.

Acknowledgements

The authors are grateful to Dr. Alan Hastie and another anonymous reviewer for their helpful comments and suggestions on the manuscript. This work was financially supported by the Natural Science Foundation of China (Nos 41472065 and 41502057) and the Foundation of Suzhou University (Nos 2015jb01, 2015jb07, KJ2017A444 and 2015SZXTZXKF05).

Appendix A. Supplementary data

Supplementary data to this article can be found online at https://doi.org/10.1016/j.lithos.2018.11.035.

References

Anderson, D.L., 2005. Large igneous provinces, delamination, and fertile mantle. Elements 1, 271–275.
Baker, M.B., Hischmann, M.M., Ghiorso, M.S., Stolper, E.M., 1995. Compositions of near-solidus peridotite melts from experiments and thermodynamic calculations. Nature 375, 308–311.
Bleeken, G.V.D., Müntener, O., Ulmer, P., 2011. Melt variability in percolated peridotite: an experimental study applied to reactive migration of tholeiitic basalt in the upper mantle. Contributions to Mineralogy and Petrology 161, 921–945.
Chen, L., Zhou, X., 2004. Ultramafic xenoliths in Mesozoic diorite in West Shandong Province. Science in China Series D 47, 489–499.
Chen, L.-H., Zhou, X.-H., 2005. Subduction-related metasomatism in the thinning lithosphere: evidence from a composite dunite-orthopyroxenite xenolith entrained in Mesozoic Laiwu high-Mg diorite, North China Craton. Geochemistry, Geophysics, Geosystems 6 Q06008.
Chen, B., Jahn, B.M., Suzuki, K., 2013. Petrological and Nd-Sr-Os isotopic constraints on the origin of high-Mg adakitic rocks from the North China Craton: Tectonic implications. Geology 41, 91–94.
Chi, S., Lu, F., Zhao, L., Zhao, C., Zheng, J.P., Deng, J., Zhang, H.F., Li, Y., Mo, X., 1996. Kimberlite in North China Craton and its Paleozoic Lithospheric Mantle. in Chinese. science press.
Fan, W.-M., Zhang, H.-F., Baker, J., Jarvis, K.E., Mason, R.P.D., Menzies, M.A., 2000. On and off the North China Craton: where is the Archaean Keel? Journal of Petrology 41, 933–950.
Fu, H., Zhu, C., 1986. Ultra-high pressure measurement technology and experimental study on mantle minerals (in Chinese). Earth and Environment 47–50.
Gao, S., Rudnick, R.L., Yuan, H.-L., Liu, X.-M., Liu, Y.-S., Xu, W.-L., Ling, W.-L., Ayers, J., Wang, X.-C., Wang, Q.-H., 2004. Recycling lower continental crust in the North China craton. Nature 432, 892–897.
Gao, S., Rudnick, R.L., Xu, W.-L., Yuan, H.-L., Liu, Y.-S., Walker, R.J., Puchtel, I.S., Liu, X., Huang, H., Wang, X.-R., Yang, J., 2008. Recycling deep cratonic lithosphere and generation of intraplate magmatism in the North China Craton. Earth and Planetary Science Letters 270, 41–53.
Gao, S., Zhang, J.F., Xu, W.L., Liu, Y.S., 2009. Delamination and destruction of the North China Craton. Chinese Science Bulletin 54, 3367–3378.
Gao, S., Takahashi, E., Suzuki, T., 2017. High-pressure Melting experiments on Basalt-Peridotite Layered Source (KLB-1/N-MORB): Implications for Magma Genesis in Hawaii. International Journal of Geosciences 8, 1–15.
Gong, C., Liu, Y., Li, P., Fan, D., Wei, S., Xie, H., 2011. Comparison of Measurement Methods for Electrical Conductivity of Rocks under High pressure and High Temperature: taken the Lherzolite as an example (in Chinese). Acta Geologica Sinica 85, 243–253.
Huang, H., Gao, S., Hu, Z., Liu, X., Yuan, H., 2007a. Geochemistry of the high-Mg andesites at Zhangwu, western Liaoning: Implication for delamination of newly formed lower crust. Science in China (Series D) 50, 1773–1786.
Huang, X.L., Xu, Y.G., Lo, C.H., Wang, R.C., Lin, C.Y., 2007b. Exsolution lamellae in a clinopyroxene megacryst aggregate from Cenozoic basalt, Leizhou Peninsula, South China: petrography and chemical evolution. Contributions to Mineralogy and Petrology 154, 691–705.
Johnston, A.D., Wyllie, P.J., 1989. The system tonalite-peridotite-H2O at 30 kbar, with applications to hybridization in subduction zone magmatism. Contributions to Mineralogy and Petrology 102, 257–264.
Kelemen, P.B., 1995. Genesis of High Mg andesites and the continental crust. Contributions to Mineralogy and Petrology 120, 1–19.
Kelemen, P.B., Hart, S.R., Bernstein, S., 1998. Silica enrichment in the continental upper mantle via melt-rock reaction. Earth and Planetary Science Letters 164, 387–406.
Kogiso, T., Hirschmann, M.M., Frost, D.J., 2003. High-pressure partial melting of garnet pyroxenite: possible mafic lithologies in the source of ocean island basalts. Earth and Planetary Science Letters 216, 603–617.
Lambart, S., Laporte, D., Provost, A., Schiano, P., 2012. Fate of Pyroxenite-derived Melts in the Peridotitic Mantle: Thermodynamic and Experimental Constraints. Journal of Petrology 53, 451–476.
Liu, Y., Gao, S., Lee, C., Hu, S., Liu, X., Yuan, H., 2005. Melt–peridotite interactions: Links between garnet pyroxenite and high-Mg# signature of continental crust. Earth and Planetary Science Letters 234, 39–57.
Liu, Y., Gao, S., Kelemen, P.B., Xu, W., 2008a. Recycled crust controls contrasting source compositions of Mesozoic and Cenozoic basalts in the North China Craton. Geochimica et Cosmochimica Acta 72, 2349–2376.
Liu, Y., Hu, Z., Gao, S., Günther, D., Xu, J., Gao, C., Chen, H., 2008b. In situ analysis of major and trace elements of anhydrous minerals by LA-ICP-MS without applying an internal standard. Chemical Geology 257, 34–43.
Ma, Q., Xu, Y.G., Zheng, J.P., Griffin, W.L., Hong, L.B., Ma, L., 2016. Coexisting early cretaceous High-Mg Andesites and Adakitic Rocks in the North China Craton: the Role of Water in Intraplate Magmatism and Cratonic Destruction. Journal of Petrology 57, 1279–1308.
Maitre, R.W.L., 1989. A Classification of Igneous Rocks and Glossary of Terms: Recommendations of the International Union of Geological Sciences Subcommission on the Systematics of Igneous Rocks. Blackwell.
Mallik, A., Dasgupta, R., 2012. Reaction between MORB-eclogite derived melts and fertile peridotite and generation of ocean island basalts. Earth and Planetary Science Letters 329-330, 97–108.
Martin, H., 1986. Effect of steeper Archean geothermal gradient on geochemistry of subduction-zone magmas. Geology 14, 753–756.
Martin, H., Smithies, R.H., Rapp, R., Moyen, J.F., Champion, D., 2005. An overview of adakite, tonalite–trondhjemite–granodiorite (TTG), and sanukitoid: relationships and some implications for crustal evolution. Lithos 79, 1–24.
Menzies, M.A., Fan, W., Zhang, M., 1993. Palaeozoic and Cenozoic lithoprobes and the loss of> 120 km of Archaean lithosphere, Sino-Korean craton, China. Geological Society, London, Special Publications 76, 71–81.
Menzies, M., Xu, Y., Zhang, H., Fan, W., 2007. Integration of geology, geophysics and geochemistry: a key to understanding the North China Craton. Lithos 96, 1–21.
Middlemost, E.A.K., 1994. Naming materials in the magma/igneous rock system. Annual Review of Earth and Planetary Sciences 37, 215–224.
Morgan, Z., Liang, Y., 2003. An experimental and numerical study of the kinetics of harzburgite reactive dissolution with applications to dunite dike formation. Earth and Planetary Science Letters 214, 59–74.
Morgan, Z., Liang, Y., 2005. An experimental study of the kinetics of lherzolite reactive dissolution with applications to melt channel formation. Contributions to Mineralogy and Petrology 150, 369–385.
Morgan, Z., Liang, Y., Hess, P., 2006. An experimental study of anorthosite dissolution in lunar picritic magmas: Implications for crustal assimilation processes. Geochimica et Cosmochimica Acta 70, 3477–3491.
Morimoto, N., 1988. Nomenclature of pyroxenes. Mineralogy and Petrology 39, 55–76.
Qi, L., Jing, H., Gregoire, D.C., 2000. Determination of trace elements in granites by inductively coupled plasma mass spectrometry. Talanta 51, 507.
Rapp, R.P., Shimizu, N., Norman, M.D., Applegate, G.S., 1999. Reaction between slab-derived melts and peridotite in the mantle wedge experimental constraints at 3.8 GPa. Chemical Geology 160, 335–356.
Rapp, R.P., Norman, M.D., Laporte, D., Yaxley, G.M., Martin, H., Foley, S.F., 2010. Continent formation in the archean and chemical evolution of the Cratonic Lithosphere: Melt–Rock Reaction experiments at 3–4 GPa and Petrogenesis of Archean Mg-Diorites (Sanukitoids). Journal of Petrology 51, 1237–1266.
Sekine, T., Wyllie, P.J., 1982. The system granite-peridotite-H2O at 30 kbar, with applications to hybridization in subduction zone magmatism. Contributions to Mineralogy and Petrology 81, 190–202.
Shaw, C.S.J., Dingwell, D.B., 2007. Experimental peridotite–melt reaction at one atmosphere: a textural and chemical study. Contributions to Mineralogy and Petrology 155, 199–214.
Sun, S.S., McDonough, W.F., 1989. Chemical and isotopic systematics of oceanic basalts: implications for mantle composition and processes. Geological Society of London, Special Publication 42, 313–345.
Sun, J., Liu, C.Z., Wu, F.Y., Yang, Y.H., Chu, Z.Y., 2012. Metasomatic origin of clinopyroxene in Archean mantle xenoliths from Hebi, North China Craton: Trace-element and Sr-isotope constraints. Chemical Geology 328, 123–136.
Tao, R., Zhang, L., Liu, X., 2015. Oxygen fugacity of Earth's mantle and deep carbon cycle in the subduction zone. Acta Petrologica Sinica 31, 1879–1890.
Tingle, T.N., Jr, H.W.G., Young, T.E., Koczynski, T.A., 1993. Improvements to Griggs-type apparatus for mechanical testing at high pressures and temperatures. Pure and Applied Geophysics 141, 523–543.
Tursack, E., Liang, Y., 2012. A comparative study of melt-rock reactions in the mantle: laboratory dissolution experiments and geological field observations. Contributions to Mineralogy and Petrology 163, 861–876.
Wang, M., Tang, H., 2013. Reaction experiments between tonalitic melt and mantle olivine and their implications for genesis of high-Mg andesites within cratons. Science China Earth Sciences 56, 1918–1925.

Wang, Y.-J., Fan, W.-M., Zhang, H.-F., Peng, T.-P., 2006. Early cretaceous gabbroic rocks from the Taihang Mountains: Implications for a paleosubduction-related lithospheric mantle beneath the central North China Craton. Lithos 86, 281–302.
Wang, C., Jin, Z.M., Gao, S., Zhang, J.F., Zheng, S., 2010. Eclogite-melt/peridotite reaction: Experimental constrains on the destruction mechanism of the North China Craton. Science China Earth Sciences 53, 797–809.
Wang, J., Hattori, K., Xu, W., Yang, Y., Xie, Z., Liu, J., Song, Y., 2012. Origin of ultramafic xenoliths in high-Mg diorites from east-Central China based on their oxidation state and abundance of platinum group elements. International Geology Review 54, 1203–1218.
Wang, C., Liang, Y., Xu, W., Dygert, N., 2013. Effect of melt composition on basalt and peridotite interaction: laboratory dissolution experiments with applications to mineral compositional variations in mantle xenoliths from the North China Craton. Contributions to Mineralogy and Petrology 166, 1469–1488.
Wang, C., Liang, Y., Dygert, N., Xu, W., 2016. Formation of orthopyroxenite by reaction between peridotite and hydrous basaltic melt: an experimental study. Contributions to Mineralogy and Petrology 171, 77.
Wu, X., Xu, Y., Ma, J.-L., Xu, J., Wang, Q., 2003. Geochemistry and petrogenesis of the Mesozoic high-Mg diorites from western Shangdong (in Chinese with Englians abstract). Geotectonica et Metallogenia 27, 228–236.
Wu, F., Xu, Y., Gao, S., Zheng, J., 2008. Lithospheric Thinning and Destruction of the North China Craton (in Chinese with English Abstract). Act a Petrologica Sinica 24. pp. 1145–1174.
Xiao, Y., Zhang, H.F., Fan, W.M., Ying, J.F., Zhang, J., Zhao, X.M., Su, B.X., 2010. Evolution of lithospheric mantle beneath the Tan-Lu fault zone, eastern North China Craton: evidence from petrology and geochemistry of peridotite xenoliths. Lithos 117, 229–246.
Xiao, Y., Zhang, H.F., Deloule, E., Su, B.X., Tang, Y.J., Sakyi, P.A., Hu, Y., Ying, J.F., 2015. Large Lithium Isotopic Variations in Minerals from Peridotite Xenoliths from the Eastern North China Craton. The Journal of Geology 123, 79–94.
Xu, Y.-G., 2001. Thermo-tectonic destruction of the archaean lithospheric keel beneath the sino-korean craton in China evidence, timing and mechanism. Physics and Chemistry of the Earth, Part A: Solid Earth and Geodesy 26, 747–757.
Xu, W., Gao, S., Wang, Q., Wang, D., Liu, Y., 2006a. Mesozoic crustal thickening of the eastern North China craton: evidence from eclogite xenoliths and petrologic implications. Geology 34, 721–724.
Xu, W.L., Yang, C., Yang, D.B., Pei, F.P., Wang, Q.H., Ji, W., 2006b. Mesozoic high-Mg diorites in eastern North China craton: constraints on the mechanism of lithospheric thinning (in Chinese with English abstract). Earth Science Frontiers 13, 120–129.
Xu, W., Hergt, J.M., Gao, S., Pei, F., Wang, W., Yang, D., 2008. Interaction of adakitic melt-peridotite: Implications for the high-Mg# signature of Mesozoic adakitic rocks in the eastern North China Craton. Earth and Planetary Science Letters 265, 123–137.
Xu, W., Yang, D.B., Pei, F.P., Yu, Y., 2009a. Petrogenesis of Fushan high-Mg# diorites from the southern Taihang Mts. in the central North China Craton: Resulting from interaction of peridotite-melt derived from partial melting of delaminated lower continental crust. Acta Petrologica Sinica 25, 1947–1961.
Xu, W.L., Gao, S., Yang, D.B., Pei, F.P., Wang, Q.H., 2009b. Geochemistry of eclogite xenoliths in Mesozoic adakitic rocks from Xuzhou-Suzhou area in Central China and their tectonic implications. Lithos 107, 269–280.
Xu, W., Wang, C., Yang, D., Wang, F., Pei, F., 2010a. Dunite xenoliths and olivine xenocrysts in gabbro from Taihang Mountains: Characteristics of Mesozoic lithospheric mantle in Central China. Journal of Earth Science 21, 692–710.
Xu, W., Yang, D., Gao, S., Pei, F., Yu, Y., 2010b. Geochemistry of peridotite xenoliths in early cretaceous high-Mg# diorites from the Central Orogenic Block of the North China Craton: the nature of Mesozoic lithospheric mantle and constraints on lithospheric thinning. Chemical Geology 270, 257–273.
Yang, C., 2007. Chronology and Geochemistry of Mesozoic High-Mg Diorite in West Shandong: Constraints on Lithospheric Evolution of the North China Craton (in Chinese with English Abstract). Jilin University.
Yaxley, G.M., Green, D.H., 1998. Reactions between eclogite and peridotite: Mantle refertilisation by subduction of oceanic crust. Schweizerische Mineralogische und Petrographische Mitteilungen 78, 243–255.
Yu, C., 2009. Ages of Peridotitic Xenoliths from Central and Eastern Areas of North China Craton and Mantle Heterogeneity (in Chinese with English Abstract). China University of Geosciences.
Yuan, H., Liu, X., Liu, Y., Gao, S., Ling, W., 2006. Geochemistry and U-Pb zircon geochronology of Late-Mesozoic lavas from Xishan, Beijing. Science in China (Series D) 49, 50–67.
Zhang, H.-F., 2005. Transformation of lithospheric mantle through peridotite-melt reaction: a case of Sino-Korean craton. Earth and Planetary Science Letters 237, 768–780.
Zhang, H.-F., Sun, M., Zhou, X.-H., Zhou, M.-F., Fan, W.-M., Zheng, J.-P., 2003a. Secular evolution of the lithosphere beneath the eastern North China Craton: evidence from Mesozoic basalts and high-Mg andesites. Geochimica et Cosmochimica Acta 67, 4373–4387.
Zhang, H.F., Sun, M., Zhou, X.H., Zhou, M.F., Fan, W.M., Zheng, J.P., 2003b. Secular evolution of the lithosphere beneath the eastern North China Craton : evidence from Mesozoic basalts and high-Mg andesites. Geochimica et Cosmochimica Acta 67, 4373–4387.
Zhang, H.-F., Nakamura, E., Sun, M., Kobayashi, K., Zhang, J., Ying, J.-F., Tang, Y.-J., Liu, L.-F., 2007. Transformation of subcontinental lithospheric mantle through peridotite-melt reaction: evidence from a highly fertile mantle xenolith from the North China craton. International Geology Review 49, 658–679.
Zhao, G., Cawood, P.A., Wilde, S.A., Lu, L., 2001. High-pressure Granulites (Retrograded Eclogites) from the Hengshan complex, North China Craton: Petrology and Tectonic Implications. Journal of Petrology 42, 1141–1170.
Zheng, J.P., Lu, F., O'Reilly, S.Y., L. Griffin, W., Zhang, M., 2000. |Mantle modification and replacement in eastern North China: a clinopyroxene laser probe study (in Chinese). Science in China (Series D) 30, 373–382.
Zheng, J., Griffin, W.L., O'Reilly, S., Liou, J.G., Zhang, R.Y., Lu, Fengxiang, 2005. Late Mesozoic-Eocene mantle replacement beneath the Eastern North China Craton: Evidence from the Paleozoic and Cenozoic Peridotite Xenoliths. International Geology Review 47, 457–472.
Zheng, J., Griffin, W.L., O'Reilly, S.Y., Yang, J., Li, T., Zhang, M., Zhang, R.Y., Liou, J.G., 2006. Mineral Chemistry of Peridotites from Paleozoic, Mesozoic and Cenozoic Lithosphere: Constraints on Mantle Evolution beneath Eastern China. Journal of Petrology 47, 2233–2256.
Zheng, J.P., Griffin, W.L., O'Reilly, S.Y., Yu, C.M., Zhang, H.F., Pearson, N., Zhang, M., 2007. Mechanism and timing of lithospheric modification and replacement beneath the eastern North China Craton: Peridotitic xenoliths from the 100 Ma Fuxin basalts and a regional synthesis. Geochimica et Cosmochimica Acta 71, 5203–5225.
Zheng, J., Wei, Y., Ping, X., Tang, H., Su, Y., Li, Y., Li, Z., Xia, B., 2016. Lower Crustal Accretion and Reworking beneath the North China Craton: Evidences from Granulite Xenoliths. Springer, Singapore.
Zi, F., He, G., Dai, S., Xu, W., 2007. Liguo Early Cretaceous High-Mg Adakitic Intrusive Rocks in the Xuzhou Region: Petrogenesis and Implications for Geodynamics and Mineralization (in Chinese with English Abstract). Acta Petrologica Sinica. 23 pp. 2857–2868.